
Article:
Sun, L., Yu, Z., Li, C. et al. (3 more authors) (2019) An imaging algorithm for spaceborne high-squint L-band SAR based on time-domain rotation. IEEE Journal of Selected Topics in Applied Earth Observations and Remote Sensing, 12 (12). pp. 5289-5299. ISSN 1939-1404

https://doi.org/10.1109/jstars.2019.2953836

An Imaging Algorithm for Spaceborne High-squint L-band SAR Based on Time-domain Rotation

Liwei Sun, Ze Yu, *Member, IEEE*, Chunsheng Li, Wei Liu, *Senior Member, IEEE*, Shusen Wang, and Jiwen Geng

***Abstract*—For spaceborne high-squint L-band synthetic aperture radar (SAR), the long wavelength and high-squint angle result in strong coupling between the range and azimuth directions. In conventional imaging algorithms, linear range walk correction (LRWC) is commonly used to correct linear range cell migration (LRCM), which dominates the coupling effect. However, LRWC introduces spatial variation in the azimuth direction, limits the depth-of-azimuth-focus (DOAF) and affects the imaging quality. This paper constructs a polynomial range model and develops a modified Omega-k algorithm to achieve spaceborne high-squint L-band SAR imaging. The key to this algorithm is to rotate the two-dimensional data after LRWC in the time domain by a proposed time-rotation (TR) operation that eliminates the DOAF degradation caused by LRWC. The proposed algorithm, which is composed of LRWC, bulk compression, TR and modified Stolt interpolation, achieves well-focused results with a one-meter resolution for a swath of 4 km × 4 km at a squint angle of 45 degrees.**

***Index Terms*—high-squint imaging, linear range walk correction (LRWC), Omega-k algorithm, synthetic aperture radar (SAR).**

I. Introduction

SYNTHETIC aperture radar (SAR) provides high azimuth resolution by exploiting the relative motion between the moving radar and its targets [1]. Due to range variations between the SAR and its target, the return echo from the target usually crosses over several range bins, an effect called range cell migration (RCM) [2], [3]. To accomplish azimuth focusing, RCM must be corrected to concentrate the echo energy into a single range bin. For spaceborne high-squint high-resolution L-band SAR, the high altitude, large squint angle, high resolution, and long wavelength result in serious coupling between the range and azimuth directions and make it necessary for the range history to be fitted by a high-order polynomial, which complicates RCM correction and SAR imaging [4]-[7].

The linear RCM (LRCM) is the dominant component in RCM for squint imaging, and it increases with the squint angle [8], [9]. To achieve more efficient and accurate imaging, LRCM is usually removed before correcting other parts of the RCM.

L. Sun, Z. Yu, C. Li, S. Wang, and J. Geng are with School of Electronic and Information Engineering, Beihang University, Beijing 100083, China (e-mail: yz613@buaa.edu.cn).

W. Liu is with Department of Electronic & Electrical Engineering, University of Sheffield, Sheffield, S1 4ET, United Kingdom. (e-mail: w.liu@sheffield.ac.uk).

Linear range walk correction (LRWC) is a commonly used method and it removes LRCM by phase compensation in the range-frequency azimuth-time domain [10]-[12]. However, LRWC leads to spatial variations in the azimuth direction, i.e., azimuth dependence, which indicates that targets in the same range bin have different Doppler frequency modulation rates [13]. Usually, an azimuth filter is designed to focus on a reference point in the swath. Due to azimuth dependence, the farther away an area is from the reference point in the azimuth direction, the greater the defocusing effect is. Therefore, the depth-of-azimuth-focus (DOAF), which refers to the azimuth distance from the reference point within which focus is considered acceptable, is limited by LRWC [14], [15].

An *et al.* presented an extended nonlinear chirp scaling algorithm based on a third-order polynomial model for X-band SAR. After LRWC, azimuth nonlinear chirp scaling is used to equalize the Doppler frequency modulation rate, alleviate the azimuth dependence, and extend the DOAF from 50 m to 5 km [16]. Sun *et al.* developed a modified range migration algorithm based on a fourth-order range model for squint sliding spotlight X-band SAR. In the first part of the algorithm, LRWC is used to correct the LRCM to facilitate subsequent operations, including deramping, azimuth resampling and phase compensation. In the second part, an inverse LRWC operation is applied to remove azimuth dependence [17]. Li *et al.* proposed an imaging approach for squint Ku-band SAR, in which cross-line-of-sight resampling in the wavenumber domain is used to correct the LRCM, and the imaging result is achieved by compensating for the first- and second-order phases [18]. However, compared with the above SAR systems, the aperture time of spaceborne high-squint L-band SAR is much longer, which causes the RCM to be larger and more complicated. Therefore, a more advanced imaging approach that can extends the DOAF under a higher-order phase condition needs to be developed.

This paper develops a modified Omega-k algorithm for spaceborne high-squint high-resolution L-band SAR that achieves a one-meter resolution for a swath of 4 km × 4 km at a squint angle of 45 degrees. The key to this algorithm is to rotate the two-dimensional data in the time domain by a proposed time-rotation (TR) operation after LRWC and bulk compression. This operation significantly improves the DOAF. Then, a modified Stolt interpolation operation is used to create the imaging results.

The remainder of this paper is structured as follows. In Section II, the echo of spaceborne high-squint L-band SAR is formulated based on a polynomial range model. In Section III, LRWC is introduced, and the DOAF degradation is analyzed. To improve

the DOAF, Section IV proposes the TR operation. Based on the TR operation, a modified Omega-k algorithm is developed in Section V. Simulation results are presented and analyzed in Sections VI. Finally, Section VII concludes the paper.

II. ECHO MODEL OF SPACEBORNE HIGH-SQUINT L-BAND SAR

The observation geometry of spaceborne squint SAR is illustrated in Fig. 1, where the origin of the coordinate system is located at the scene center P_{ref}, and the X, Y, and Z axes represent the azimuth, range and geocentric directions, respectively.

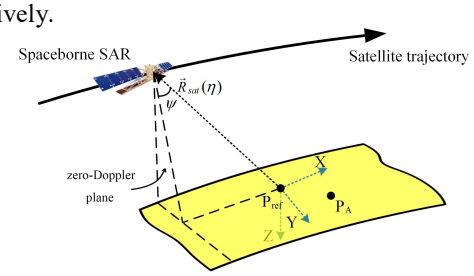

(a)

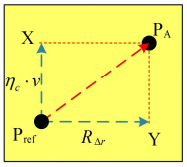

(b)

Fig. 1. Illustrations of the observation geometry (a) and the observed scene (b). P_{ref} is the origin of the coordinate system, located at the scene center; *X*, *Y*, and *Z* axes represent the azimuth, range, and geocentric directions, respectively. Ψ is the squint angle for the reference point at the beam center crossing time. P_A denotes a target at $(\eta_c v, R_{\Delta r}, 0)$. The spaceborne SAR flies along the satellite trajectory, and $\vec{R}_{sat}(\eta)$ is the position vector of the SAR.

Suppose that a chirp signal is transmitted. After demodulation, the echo from the isolated point target P_A at $(\eta_c v, R_{\Delta r}, 0)$ can be represented by

$$s(\tau,\eta) = w_\tau\left[\tau - 2R(\eta,\eta_c,R_{\Delta r})/c\right] w_\eta(\eta-\eta_c) \times \exp\left\{j\pi\gamma\left[\tau - 2R(\eta,\eta_c,R_{\Delta r})/c\right]^2\right\} \exp\left[-j4\pi R(\eta,\eta_c,R_{\Delta r})/\lambda\right], \quad (1)$$

where η and τ denote the azimuth and range time, respectively, $w_\eta(\eta)$ and $w_\tau(\tau)$ represent the azimuth and range weighting, respectively, c is the speed of light, λ is the wavelength, γ is the linear frequency modulation rate of the transmitting signal. Here, v is the speed of the moving SAR platform, η_c is the beam center crossing time corresponding to P_A, and $R(\eta,\eta_c,R_{\Delta r})$ denotes the slant range between SAR and P_A, which equals

$$R(\eta,\eta_c,R_{\Delta r}) = \left|\vec{R}_{sat}(\eta) - (\eta_c v, R_{\Delta r}, 0)\right|, \quad (2)$$

where $\vec{R}_{sat}(\eta)$ is the position vector of the satellite, and $|\cdot|$ denotes the modulus of a vector. (2) can also be approximated as follows (see Appendix I):

$$R(\eta,\eta_c,R_{\Delta r}) \approx \sum_{n=0}^{N} B_n(\eta-\eta_c)^n, \quad (3)$$

where B_n is spatially variant in the range direction and can be expressed as

$$\begin{cases} B_0 = r_{00} + r_{01}R_{\Delta r} + \cdots + r_{0M}R_{\Delta r}^M \\ B_1 = r_{10} + r_{11}R_{\Delta r} + \cdots + r_{1M}R_{\Delta r}^M \\ \cdots \\ B_N = r_{N0} + r_{N1}R_{\Delta r} + \cdots + r_{NM}R_{\Delta r}^M \end{cases}, \quad (4)$$

and r_{nm} can be calculated by polynomial fitting based on the ephemeris data and the geographic information in the scene, and it is spatially invariant in the range direction. With $R_{\Delta r}=0$, $B_n = r_{n0}$, which indicates that r_{n0} is the polynomial coefficient in (3) for targets in the same range gate as the reference point (the center of the swath). As a result, r_{10} is independent of $R_{\Delta r}$. For broadside SAR, which has zero-Doppler centroid, (3) with N=4 is adequate to approximate the slant range [19], in the case of L-band and a resolution of one meter. However, in the high-squint case, the nonzero squint angle results in a smaller Doppler rate [20]. To form the same Doppler bandwidth and azimuth resolution, the aperture time of squint SAR should be longer than that of broadside SAR. Therefore, the orders of (3) and (4) must be sufficiently high to describe the more complicated relative motion over the longer aperture time. *N* and *M* are set to 6 and 4 in the paper, respectively, which will be validated in Section 6.2.

The amount of RCM is the difference between the maximum and minimum values of (3), equal to

$$\Delta_{RCM} = \left|\sum_{n=odd}^{N}\left(\sum_{m=0}^{M} r_{nm}R_{\Delta r}^m\right)2(T_a/2)^n\right|, \quad (5)$$

for high-squint SAR. T_a represents the aperture time. The spatially invariant term $r_{10}T$, which is part of LRCM, occupies the vast majority of the RCM. As shown in Fig. 2, the ratio of $r_{10}T$ to Δ_{RCM} exceeds 90% when the squint angle reaches 45 degrees. The phase related to r_{10} in (1) skews the spectrum and causes the azimuth spectrum to deviate from the baseband, as shown in Fig. 3. Therefore, for high-squint SAR, correcting the term around r_{10} is necessary to reduce the range-azimuth coupling and move the azimuth spectrum back to the baseband.

III. LRWC AND DOAF DEGRADATION

In squint SAR imaging, LRWC is commonly used to compensate for the spatially invariant term $r_{10}\eta$ in (1) [21]-[23].

By transforming (1) into the range frequency domain, the signal becomes

$$s(f_\tau,\eta) = \exp\left[-j4\pi(f_0+f_\tau)R(\eta,\eta_c,R_{\Delta r})/c\right]\exp\left(-j\pi f_\tau^2/\gamma\right), \quad (6)$$

where f_τ and f_0 denote the range frequency and the carrier frequency, respectively.

The LRWC filter is designed as follows:

$$H_{LRWC}(f_\tau,\eta) = \exp\left(j4\pi f_0 r_{10}\eta/c\right)\exp\left(j4\pi f_\tau r_{10}\eta/c\right), \quad (7)$$

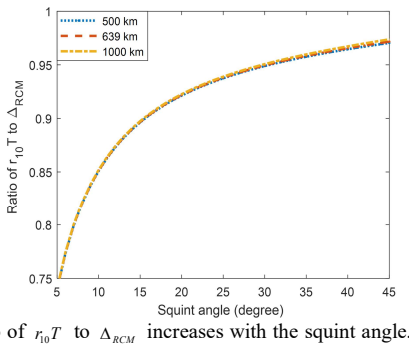

Fig. 2. Ratio of $r_{10}T$ to Δ_{RCM} increases with the squint angle. The curves are obtained for L-band SAR with a resolution of one meter and orbital heights of 500, 639 and 1000 km.

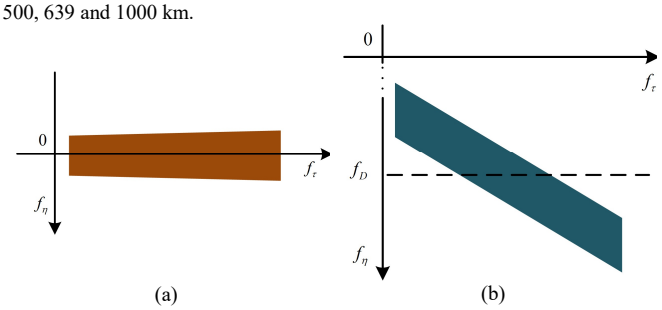

(a) (b)

Fig. 3. Impact of the phase related to r_{10} on the spectrum. f_η and f_τ denote the azimuth and range frequencies, respectively. f_D represents the Doppler centroid. The spectrums corresponding to broadside and squint SARs are illustrated in (a) and (b), respectively. The term r_{10} not only makes f_D nonzero but also skews the spectrum, which increases the difficulty of imaging.

where the first term moves the azimuth spectrum back to the baseband, and the second causes the spectrum to no longer be distorted.

After LRWC, the signal becomes

$$s_{LRWC}(f_\tau,\eta)=\exp\left\{-j4\pi(f_0+f_\tau)\left[R(\eta,\eta_c,R_{\Delta r})-r_{10}(\eta-\eta_c)\right]/c\right\}\times\exp\left(-j\pi f_\tau^2/\gamma\right)\exp\left[j4\pi(f_0+f_\tau)r_{10}\eta_c/c\right] \quad (8)$$

Based on the method of series reversion (MSR) [24], (8) can be expressed in the wavenumber domain, which is (see Appendix II)

$$\begin{aligned}s_{LRWC}(k_\eta,\Delta k_\tau)&=\exp\left\{j\theta(k_\eta,\Delta k_\tau)\right\}\\&\approx\exp\left\{j\left[P_0(k_\eta,\Delta k_\tau)+P_1(k_\eta,\Delta k_\tau)R_{\Delta r}\right]\right\}\\&\times\exp\left(-jk_\eta v\eta_c\right)\exp\left(j\Delta k_\tau r_{10}\eta_c\right)\exp\left(jk_{\tau c}r_{10}\eta_c\right)\end{aligned}, \quad (9)$$

where $k_\eta=f_\eta 2\pi/v$, $k_{\tau c}=4\pi f_0/c$, and $\Delta k_\tau=4\pi f_\tau/c$. and

$$\begin{cases}P_0(k_\eta,\Delta k_\tau)=\left[\theta(k_\eta,\Delta k_\tau)+k_\eta v\eta_c-(k_{\tau c}+\Delta k_\tau)r_{10}\eta_c\right]\Big|_{R_{\Delta r}=0}\\P_1(k_\eta,\Delta k_\tau)=\dfrac{\partial\theta(k_\eta,\Delta k_\tau)}{\partial R_{\Delta r}}\Big|_{R_{\Delta r}=0}\end{cases}.$$

To compensate for the spatially invariant term $P_0(k_\eta,\Delta k_\tau)$ in (9), the bulk compression filter $H_{bulk}(k_\eta,\Delta k_\tau)$ is used:

$$H_{bulk}(k_\eta,\Delta k_\tau)=\exp\left[-jP_0(k_\eta,\Delta k_\tau)\right]. \quad (10)$$

Then, the signal becomes

$$\begin{aligned}s_{bluk}(k_\eta,\Delta k_\tau)&=\exp\left[jP_1(k_\eta,\Delta k_\tau)R_{\Delta r}\right]\\&\times\exp\left(-jk_\eta v\eta_c\right)\exp\left(j\Delta k_\tau r_{10}\eta_c\right)\exp\left(jk_{\tau c}r_{10}\eta_c\right)\end{aligned}. \quad (11)$$

By applying Stolt interpolation [25], $P_1(k_\eta,\Delta k_\tau)$ can be mapped into a new wavenumber $(k_{\tau c}+\Delta k'_\tau)$, which indicates that

$$P_1(k_\eta,\Delta k_\tau)=(k_{\tau c}+\Delta k'_\tau). \quad (12)$$

Equation (11) can be expressed as follows: (see Appendix III)

$$\begin{aligned}s_{stolt}(k_\eta,\Delta k'_\tau)&=\exp\left[j(k_{\tau c}+\Delta k'_\tau)R_{\Delta r}\right]\\&\times\exp\left(-jk_\eta v\eta_c\right)\exp\left[j\Delta\Phi(k_\eta,\Delta k'_\tau)\right]\exp\left(jk_{\tau c}r_{10}\eta_c\right)\end{aligned}, \quad (13)$$

where

$$\Delta\Phi(k_\eta,\Delta k'_\tau)=\exp\left[j\sum_{h=1}^{H}A_h\left[(k_{\tau c}+\Delta k'_\tau)-P_1(k_\eta,\Delta k_\tau)\Big|_{\Delta k_\tau=0}\right]^h r_{10}\eta_c\right]. \quad (14)$$

Finally, A_h can be calculated based on MSR, and the expressions are illustrated in Appendix III.

If $\Delta\Phi(k_\eta,\Delta k'_\tau)$ satisfies

$$\left.\frac{\partial^2\Delta\Phi(k_\eta,\Delta k'_\tau)}{2(\partial k_\eta)^2}\right|_{k_\eta=0}\left(\frac{B_\eta}{2}\right)^2>\pi/4, \quad (15)$$

which indicates that the maximum quadratic phase error (QPE) determined by $\Delta\Phi(k_\eta,\Delta k'_\tau)$ is greater than $\pi/4$, the QPE causes clear defocusing effects on the imaging result. Here, B_η is the Doppler bandwidth. Because QPE increases with $|\eta_c|$, which is proportional to the azimuth position of the target, only those targets within a limited azimuth swath width can avoid the situation described by (15) and achieve good focus. This width is called the DOAF, calculated as (see Appendix IV)

$$L_{DOAF}<\left[50r_{20}^2(r_{01}-r_{10}r_{11}/(2r_{20}))v\right]/(r_{21}B_\eta^2 r_{10}). \quad (16)$$

As illustrated in Fig. 4, defocusing is clearly present in the area outside the DOAF. It is desirable to have the DOAF as large as possible. By comparing (6), (8), and (9), the LRWC operation results in a linear phase $\exp(j\Delta k_\tau r_{10}\eta_c)$ in (11), and further generates $\Delta\Phi(k_\eta,\Delta k'_\tau)$ in (13), which leads to DOAF degradation. Therefore, $\exp(j\Delta k_\tau r_{10}\eta_c)$ should be corrected before Stolt interpolation to improve the DOAF.

IV. DOAF IMPROVEMENT USING TIME ROTATION

In this section, a time rotation (TR) method is proposed to maintain the advantage of LRWC and improve the DOAF. By transforming (11) back into the two-dimensional time domain, we obtain

$$\begin{aligned}s_{bulk}(\tau,\eta)&=\int_{-\infty}^{\infty}w_\eta(u-\eta_c)\exp\left[-j4\pi R'(u,\eta_c,R_{\Delta r})/\lambda\right]\\&\times\exp\left[j4\pi R'(u-\eta,\eta_c,0)/\lambda\right]du\\&\times T_r\sin c\left\{\gamma T_r\left[\tau-2R'(\eta,\eta_c,R_{\Delta r})/c+2r_{10}\eta_c/c\right]\right\}\end{aligned}, \quad (17)$$

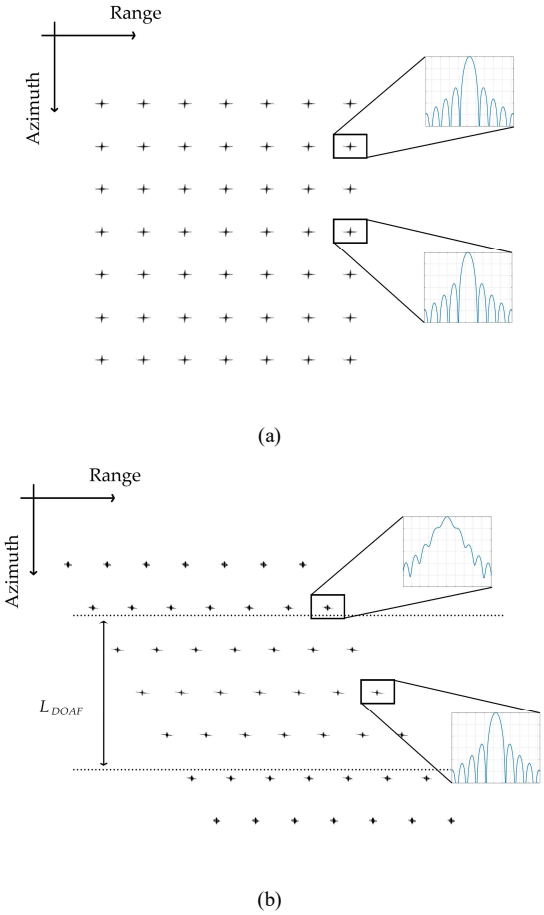

Fig. 4. Illustration of the DOAF. The imaging results of a simulation scene that includes 7×7 point targets in the broadside and squint modes are demonstrated in (a) and (b), respectively. Because LRWC is used in squint imaging, clear defocusing appears outside the DOAF. In contrast, there is no DOAF limitation in the broadside image.

where $R'(\eta,\eta_c,R_{\Delta r})=R(\eta,\eta_c,R_{\Delta r})-r_{10}\cdot(\eta-\eta_c)$, and it is the residual range migration after $r_{10}(\eta\text{-}\eta_c)$ is compensated for by LRWC. T_r is the pulse width. When $R_{\Delta r}=0$, (17) becomes

$$s_{bulk}(\tau,\eta)\big|_{R_{\Delta r}=0}=T_aT_r\sin c\left[-(4B_2/\lambda)T_a(\eta-\eta_c)\right]\times\sin c\left\{\gamma T_r\left[\tau-2R'(\eta,\eta_c,R_{\Delta r})/c+2r_{10}\eta_c/c\right]\right\}. \quad (18)$$

By comparing (17) and (18), it can be concluded that only targets with $R_{\Delta r}=0$ are well focused, while other targets are defocused after LRWC and bulk compression.

Fig. 5(a) illustrates some point targets in the observed scene. The center point P_{ref} is located at the scene center, and all the brown targets are in the same range gate, with $R_{\Delta r}=0$. Fig. 5(b) demonstrates the result after LRWC and bulk compression, where only the brown-colored targets are focused. Due to the phase $\exp(j\Delta k_\tau r_{10}\eta_c)$ induced by LRWC, other than the scene center, each target has a range offset $\Delta\tau$:

$$\Delta\tau=2r_{10}\eta_c/c. \quad (19)$$

To compensate for the linear phase term $\exp(j\Delta k_\tau r_{10}\eta_c)$ in (11) and improve the DOAF, the basic idea of TR is to rotate the data by a specific angle θ to correct the range offset $\Delta\tau$, as

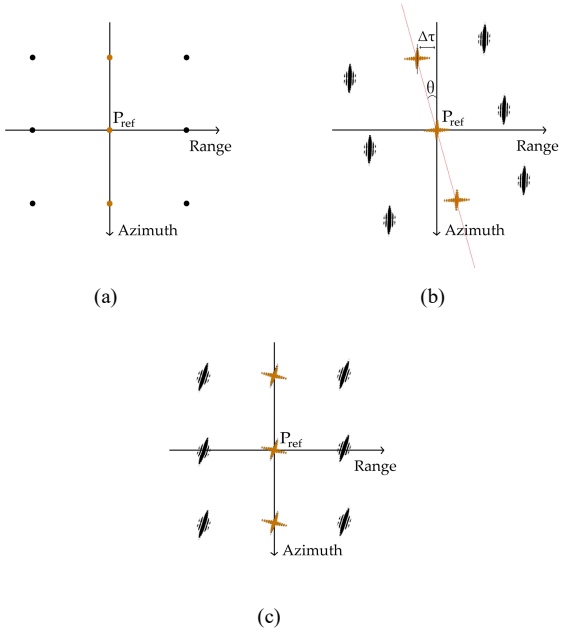

Fig. 5. Illustration of TR. The simulation scene is shown in (a), and a simulated echo is generated. The processing result after LRWC and bulk compression is shown in (b). After further performing the TR operation, the result is shown in (c). In both (b) and (c), the brown-colored targets are focused, and the other targets are defocused.

illustrated in Fig. 5(c). The rotation in the time domain can be expressed as follows:

$$\begin{bmatrix}X'_\eta\\X'_\tau\end{bmatrix}=\begin{bmatrix}\cos\theta&\sin\theta\\-\sin\theta&\cos\theta\end{bmatrix}\begin{bmatrix}X_\eta\\X_\tau\end{bmatrix}, \quad (20)$$

where $X_\eta=\eta v$, $X_\tau=\tau c/2$. After TR, the signal in the wavenumber domain becomes

$$s_{TR}(k_\eta,\Delta k_\tau)=\exp\left[jQ(k_\eta,\Delta k_\tau)R_{\Delta r}\right]\exp\left[j(\sin\theta r_{10}\eta_c-\cos\theta v\eta_c)k_\eta\right]\times\exp\left[j(\sin\theta v\eta_c+\cos\theta r_{10}\eta_c)\Delta k_\tau\right]\exp(jk_{\tau c}r_{10}\eta_c). \quad (21)$$

where

$$Q(k_\eta,\Delta k_\tau)=P_1\left\{(\cos\theta k_\eta-\sin\theta\Delta k_\tau),(\sin\theta k_\eta+\cos\theta\Delta k_\tau)\right\}.$$

By comparing (11) and (21), the linear phase term of Δk_τ caused by LRWC should be cancelled to eliminate the DOAF limitation. Therefore, the following equation should be satisfied.

$$\sin\theta v\eta_c+\cos\theta r_{10}\eta_c=0. \quad (22)$$

The rotation angle θ is solved as follows:

$$\theta=\arctan(-r_{10}/v). \quad (23)$$

By substituting (23) into (21), (21) can be simplified as

$$s_{TR}(k_\eta,\Delta k_\tau)=\exp\left[jQ(k_\eta,\Delta k_\tau)R_{\Delta r}\right]\times\exp\left[j(\sin\theta r_{10}\eta_c-\cos\theta v\eta_c)k_\eta\right]\exp(jk_{\tau c}r_{10}\eta_c). \quad (24)$$

Then, the linear phase of Δk_τ disappears and the DOAF limitation induced by LRWC is eliminated.

V. MODIFIED OMEGA-K ALGORITHM FOR SPACEBORNE HIGH-SQUINT L-BAND SAR

Combined with TR, a modified Omega-k algorithm is proposed to accomplish spaceborne high-squint L-band SAR imaging, as demonstrated in Fig. 6. The detailed steps are as follows.

1) The coefficients r_{nm} in (4) can be obtained by means of polynomial fitting based on ephemeris data and geographic information of the scene. The LRWC filter is constructed according to (7). A Fourier transform along the range and LRWC filtering are then implemented successively on the SAR echo to obtain $s_{LRWC}\left(k_\eta,\Delta k_\tau\right)$, which has the same expression as (9).

2) The bulk compression filter $H_{bulk}\left(k_\eta,\Delta k_\tau\right)$ is designed according to (10). By multiplying $s_{LRWC}\left(k_\eta,\Delta k_\tau\right)$ and $H_{bulk}\left(k_\eta,\Delta k_\tau\right)$, $s_{bluk}\left(k_\eta,\Delta k_\tau\right)$ can be achieved as in (11).

3) $s_{bulk}\left(\tau,\eta\right)$ is obtained by transforming $s_{bluk}\left(k_\eta,\Delta k_\tau\right)$ into a two-dimensional domain. The azimuth sampling rate is adjusted by zero padding in a two-dimensional frequency domain to ensure that the sampling intervals are equal in both the range and azimuth directions. The new azimuth-sampling rate is

$$PRF_{new}=2f_s v/c\,. \tag{25}$$

where f_s denotes the range sampling frequency. Then the TR operation is carried out in 2-D time domain.

4) The modified Stolt interpolation is implemented as

$$Q\left(k_\eta,\Delta k_\tau\right)=\left(k_{\tau c}+\Delta k'_\tau\right). \tag{26}$$

Then, (24) becomes

$$\begin{aligned}s_{stolt}\left(k_\eta,\Delta k'_\tau\right)&=\exp\left[j\left(k_{\tau c}+\Delta k'_\tau\right)R_{\Delta r}\right]\\&\times\exp\left[j\left(\sin\theta r_{10}\eta_c-\cos\theta v\eta_c\right)k_\eta\right]\exp\left(jk_{\tau c}r_{10}\eta_c\right)\end{aligned}. \tag{27}$$

By transforming (27) into the two-dimensional time domain, the focused imaging result can be obtained as follows:

$$\begin{aligned}s_{stolt}\left(\tau,\eta\right)&=T_aT_r\sin c\left[\gamma T_r\left(\tau+2R_{\Delta r}/c\right)\right]\\&\times\sin c\left\{-\left(4B_2T_a/\lambda\right)\left[\eta-\eta_c\cdot\sqrt{r_{10}{}^2+v^2}/v\right]\right\}\end{aligned}. \tag{28}$$

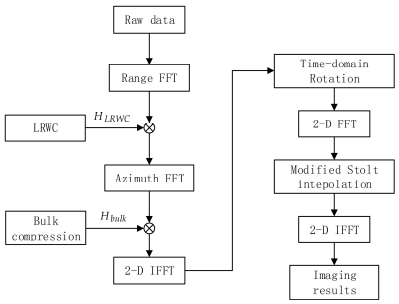

Fig. 6. Flowchart of the proposed modified Omega-k algorithm based on TR.

VI. SIMULATION AND ANALYSIS

A. Simulation Parameters

The parameters used in the simulation are listed in Table I. The simulated scene covers an area of 4 km × 4 km as shown in Fig. 7, where three point targets are arranged in the swath. P_2 is located at the center of the imaging scene, P_1 and P_3 are at the upper left and lower right corners of the scene, respectively.

TABLE I
SIMULATION PARAMETERS

Parameters	Value
Carrier frequency (GHz)	1.3
Range bandwidth (MHz)	150
Sampling frequency (MHz)	216
Pulse width (μs)	60
Pulse repetitive frequency (Hz)	9996
Orbital height (km)	639
Platform velocity (m/s)	7613
Aperture time (s)	41
Squint angle (°)	45
Resolution (m)	1

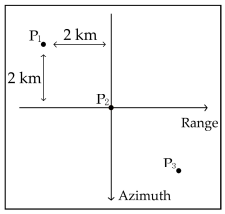

Fig. 7. Simulated scene. The scene size is 4 km × 4 km. P_2 is at the scene center, and P_1 and P_3 are at the upper-left and lower-right corners, respectively.

B. Validation of the Range Model

For spaceborne high-squint L-band SAR, the aperture time is long, and the order of the range model must be sufficiently high to describe the echo precisely and guarantee the imaging quality. In this study, we construct a polynomial range model (PRM) in which N and M are set to 6 and 4 in (3) and (4), respectively. We validate the PRM by comparing it with commonly used range models, including the modified equivalent range model (MERM), the fourth-order Doppler range model (DRM4) and the modified advanced hyperbolic range equation (MAHRE).

Fig. 8 demonstrates the phase errors induced by the different models for the center target P_2 and edge target P_1. The phase errors increase with the aperture time. To achieve one meter resolution, the aperture time reaches 41 seconds for spaceborne high-squint L-band SAR imaging at the squint angle of 45 degrees. In this case, only the PRM reduces the phase error to less than $\pi/4$, which indicates that the imaging quality is almost unaffected [20], but DRM4, MERM, and MAHRE have failed. Therefore, the PRM is appropriate for this study.

C. Imaging Results and Analysis

Simulation results of the proposed algorithm and the algorithm in [18] are achieved based on the parameters listed in Table I. Figs. 9 and 10 demonstrate the contour maps and azimuth profiles of the imaging results. Each figure shows two types of results. The first column is achieved using the algorithm in [18], which has good squint imaging ability and accomplished the airborne SAR imaging task with a 0.5-meter

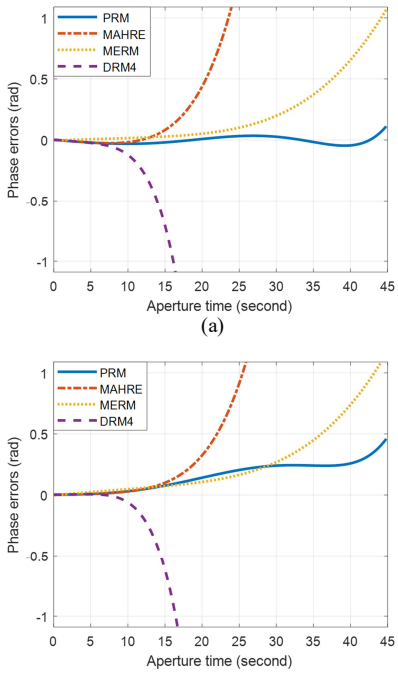

Fig. 8. Phase errors induced by different range models for the center target P_2 and edge target P_1 are illustrated in (a) and (b).

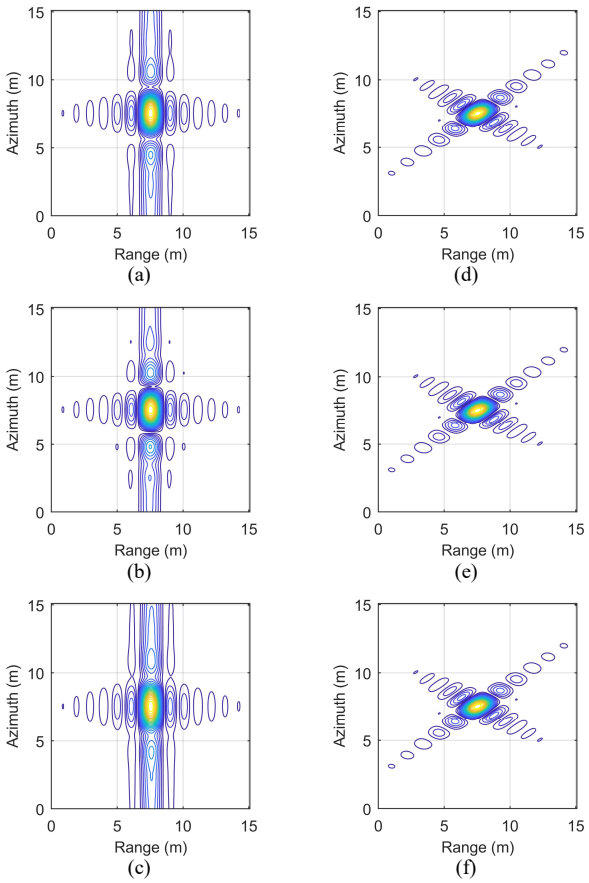

Fig. 9. Contour maps: (a), (b), and (c) are the contour maps of P_1, P_2, P_3 achieved by the algorithm in [18], whereas (d), (e), and (f) are those of P_1, P_2, P_3 achieved by the proposed method.

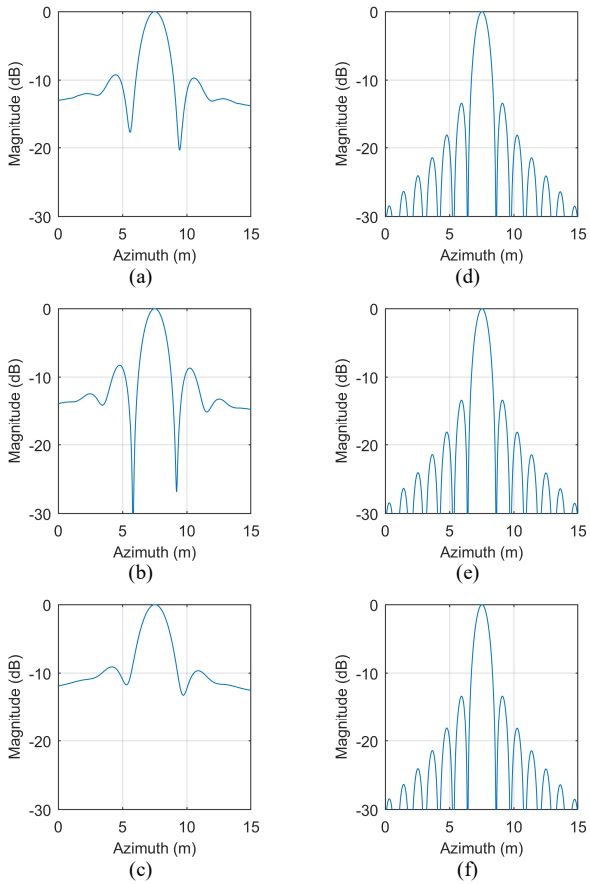

Fig. 10. Azimuth profiles: (a), (b), and (c) are the azimuth profiles of P_1, P_2, P_3 achieved by the algorithm in [18], whereas (d), (e), and (f) are those achieved by the proposed method.

resolution and 75 degrees squint angle. The second column is achieved by the modified Omega-k algorithm proposed in this paper. In both figures, the first, second, and third rows correspond to P_1, P_2, and P_3, respectively. As illustrated in Fig. 9, there is no difference between the range focusing quality achieved by these two algorithms. Therefore, the range profiles are not presented here.

Using resolution, peak-to-side-lobe ratio (PSLR), and integrated side-lobe ratio (ISLR) as indicators to evaluate Fig. 10, the results in azimuth are presented in Table II.

TABLE II
EVALUATION RESULTS IN AZIMUTH

Methods	Target	Resolution (m)	PSLR (dB)	ISLR (dB)
Reference method	P_1	1.78	-9.21	0.84
	P_2	1.57	-8.25	0.64
	P_3	1.98	-9.06	0.99
Proposed method	P_1	1.00	-13.32	-10.50
	P_2	1.00	-13.34	-10.53
	P_3	1.00	-13.33	-10.52

The algorithm proposed in [18] can achieve perfect imaging performance for Ku-band airborne SAR with azimuth resolution of 0.5m. However, in the case of spaceborne SAR, the third and higher-order phases ignored in [18] broadens the main lobe and

deteriorates the azimuth resolution, PSLR, and ISLR, as shown

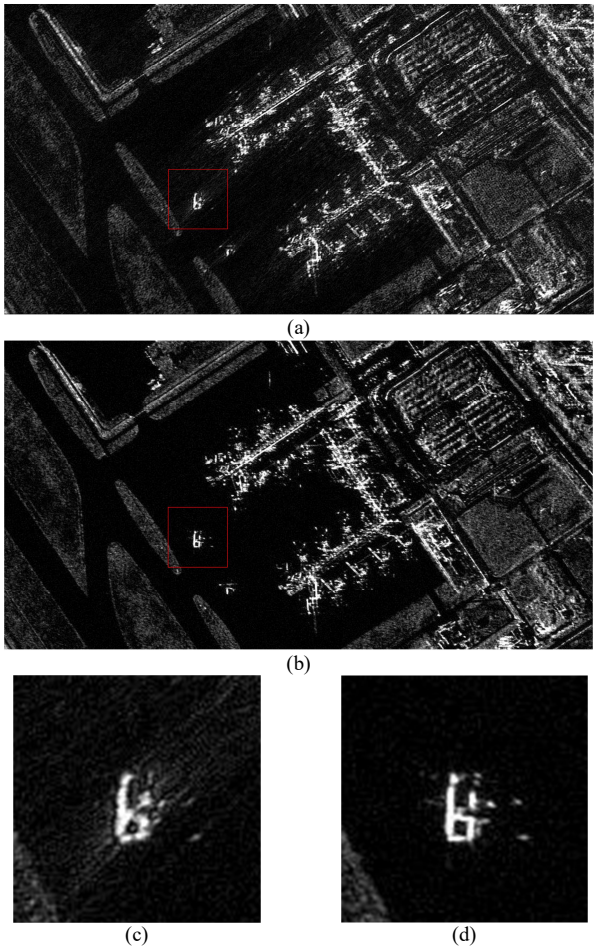

Fig. 11. Imaging results of real scene: (a) is the result of the algorithm in [18], (b) is the result of the proposed method, whereas (c), (d) are the partial enlarged detail of (a) and (b), respectively.

in Table II.

The proposed algorithm achieves better imaging quality. It improves the azimuth resolution, PSLR, and ISLR by approximately 36.3%, 4.11 dB, and 11.17 dB, respectively, and its focusing qualities for P_1, P_2, and P_3 are nearly the same, which indicates good imaging coherency for the whole swath.

The imaging results of the real scene, the Zhuhai Airport in south China, are shown in Fig. 11. This scene includes lawn, plans, and buildings, and can directly reflect the imaging performance of two algorithms. Images (a) and (c) are from the reference algorithm in [18], images (b) and (d) are from the proposed algorithm. It's obvious that the images from the reference algorithm have more serious sidelobe effect, which may cause a false alarm and reduce the ability to detect weak targets.

D. Constraint on Scene Dimension and Solutions

As mentioned above, the algorithm proposed in this paper can achieve good imaging quality for high-squint L-band SAR. However, a limitation exists for the proposed algorithm. Equation (9) ignores a portion of the phases about $R_{\Delta r}$, which equals

$$\Phi_h = \exp\left[j\sum_{m=2}^{M} P_m\left(k_\eta, \Delta k_\tau\right) R_{\Delta r}^m \right]. \tag{29}$$

After Stolt interpolation, the omission of (29) results in the following QPE:

$$QPE_h \approx \left[0.016 r_{11} r_{21}^{\ 2} r_{10} \middle/ \left(r_{01} r_{20}^{\ 4}\right)\right]\left(B_\eta/2\right)^2 R_{\Delta r}^2 . \tag{30}$$

The value of QPE_h grows with $R_{\Delta r}$, as shown in Fig. 12(a). The quality of the focused image deteriorates when QPE_h is greater than $\pi/4$. Let (30) be less than $\pi/4$, and the unilateral swath size in the range direction should satisfy

$$R_{\Delta r} < \sqrt{\pi r_{01} r_{20}^{\ 4} \middle/ \left(0.016 r_{11} r_{21}^{\ 2} r_{10} B_\eta^{\ 2}\right)} . \tag{31}$$

Using the simulation parameters in Table I, swath size is less than 6 km.

When the swath size is larger than the limitation determined by (31), the entire echo data must be segmented in the range direction to make each chunk of subswath data satisfy (31). The *i*th subswath is compensated for by

$$H_{ci} = \exp\left[-j\sum_{m=2}^{M} P_m\left(k_\eta, \Delta k_\tau\right) R_{\Delta r i}^m \right], \tag{32}$$

where $R_{\Delta r i}$ represents the distance from the center of the whole swath to that of the *i*th subswath. By implementing segmentation and applying (32) before Stolt interpolation, QPE_h will be small enough to guarantee the imaging quality for the entire swath, as shown in Fig. 12(b).

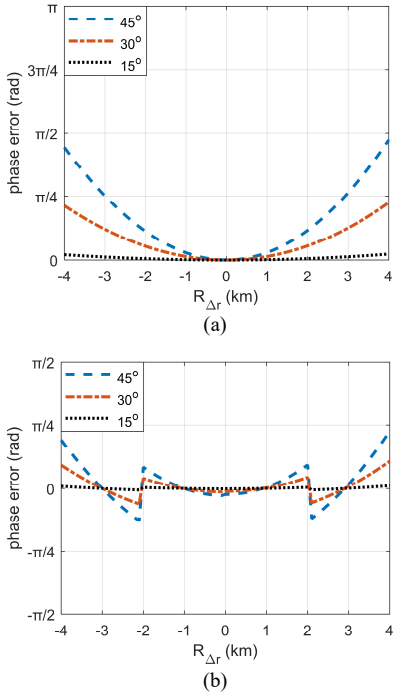

Fig. 12. Variation of phase errors with $R_{\Delta r}$. The results are achieved using the parameters in Table I and squint angles of 15, 30 and 45 degrees. The phase error corresponding to (30) is shown in (a). After segmentation and compensation by applying (32), the residual phase error is illustrated in (b).

E. Computational Load

This part mainly analyses the computational load advantages of the proposed algorithm in high squint case. Suppose M_F and N_F denote the azimuth and range pixel numbers of the final imaging result, respectively, and the original echo sizes are M_R and N_R. For a normal algorithm without LRWC, the computational load can be expressed as

$$2M_R N_R \log_2(N_R M_R) + 17 M_R N_R . \tag{33}$$

For the proposed algorithm, since LRWC compensates for the linear range cell migration, the range size of the data can be significantly reduced by applying LRWC. Based on the parameters in Table I, the range size is reduced to 1/42 of the original. As a result, the amount of computation becomes less. According to the flowchart in Fig. 6, the computational load can be written as

$$M_R N_R(\log_2 N_R + 1) + 2M_F N_F \log_2(N_F M_F) + (M_F + 80N_F) N_F . \tag{34}$$

The computational load of the reference algorithm in [18] with the same data size is given as

$$M_R N_R\left[\frac{1}{2}\log_2(N_R M_R) + 19\right] + M_F N_F\left[\frac{1}{2}\log_2(N_F M_F) + 19\right]. \tag{35}$$

Fig. 13 shows the variation of the computational load with the squint angle. It can be seen that the computational load of the proposed algorithm is the lowest, especially in high squint cases.

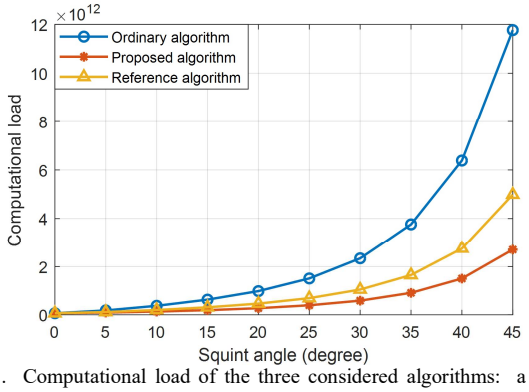

Fig. 13. Computational load of the three considered algorithms: a normal algorithm without LRWC, the proposed algorithm and the reference algorithm.

VII. CONCLUSION

Spaceborne high-squint L-band synthetic aperture radar (SAR) has good temporal coherence and penetration capability and is suitable for ecological surveillance, such as surveys of phytomass and soil moisture [26]-[28]. The high-squint mode also enables it to obtain backscattering information of the target region from multiple angles [29]. In this paper, a modified Omega-k algorithm is developed based on TR which eliminates the DOAF limitation caused by LRWC. Simulation results have shown that the proposed algorithm can achieve well-focused results with a one-meter resolution for a swath of 4 km × 4 km at a squint angle of 45 degrees. Compared with the algorithm in [18], the proposed one improves the azimuth resolution, PSLR, and ISLR by approximately 36.3%, 4.11 dB, and 11.17 dB, respectively. The proposed algorithm allows SAR to be used at different squint angles to achieve more target region acquisitions in a single pass, so that changes can be detected by exploiting sequential images.

APPENDIX I

$R(\eta,\eta_c,R_{\Delta r})$ denotes the slant range between the satellite and a target, given by

$$R(\eta,\eta_c,R_{\Delta r}) = \sqrt{\left\langle \vec{R}_{sat}(\eta) - \vec{R}_{\Delta\eta} - \vec{R}_{\Delta r}, \vec{R}_{sat}(\eta) - \vec{R}_{\Delta\eta} - \vec{R}_{\Delta r} \right\rangle}, \tag{36}$$

where $\vec{R}_{\Delta\eta} = \eta_c v\vec{x}$, and $\vec{R}_{\Delta r} = R_{\Delta r}\vec{y}$. Equation (36) can be expressed as follows:

$$R(\eta,\eta_c,R_{\Delta r}) = \sqrt{\left\langle \vec{R}_{sat}(\eta-\eta_c) - \vec{R}_{\Delta r}, \vec{R}_{sat}(\eta-\eta_c) - \vec{R}_{\Delta r} \right\rangle}. \tag{37}$$

Then, the following expression can be obtained:

$$R(\eta,\eta_c,R_{\Delta r}) = \sqrt{\left|\vec{R}_{sat}(\eta-\eta_c)\right|^2 + \left|\vec{R}_{\Delta r}\right|^2 - 2\cdot\left\langle \vec{R}_{sat}(\eta-\eta_c), \vec{R}_{\Delta r} \right\rangle}. \tag{38}$$

Because $R_{ref}(\eta) >> \left|\vec{R}_{\Delta r}\right|$, where $R_{ref}(\eta)$ denotes the range history of a target on the center of the scene, and $R(\eta,\eta_c,R_{\Delta r}) >> \left|\vec{R}_{\Delta r}\right|$, (38) can be approximated as follows:

$$R(\eta,\eta_c,R_{\Delta r}) \approx R_{ref}(\eta-\eta_c) - \left\langle \vec{R}_{sat}(\eta-\eta_c), \vec{R}_{\Delta r} \right\rangle / R_0 , \tag{39}$$

where R_0 denotes the slant distance corresponding to the reference point at the beam center crossing time. The satellite position vector $\vec{R}_{sat}(\eta)$ can be represented by

$$\vec{R}_{sat}(\eta-\eta_c) = \sum_{n=0}^{\infty} \frac{1}{n!} \vec{R}_{sat}^{(n)}\Big|_{\eta=\eta_c} (\eta-\eta_c)^n , \tag{40}$$

where $\vec{R}_{sat}^{(n)}\Big|_{\eta=\eta_c}$ denotes the nth-order derivative of $\vec{R}_{sat}(\eta)$ at $\eta=\eta_c$. By substituting (40) into (39), we obtain the following result:

$$R(\eta,\eta_c,R_{\Delta r}) = R_{ref}(\eta-\eta_c) - \frac{1}{R_0}\sum_{n=0}^{\infty}\frac{1}{n!}\left\langle \vec{R}_{sat}^{(n)}\Big|_{\eta=\eta_c}, \vec{R}_{\Delta r} \right\rangle (\eta-\eta_c)^n , \tag{41}$$

Then, (41) can be simplified to

$$R(\eta,\eta_c,R_{\Delta r}) = B_0 + \sum_{n=1}^{\infty} B_n (\eta-\eta_c)^n , \tag{42}$$

where

$$B_n = B_{n\_ref} - \left\langle \vec{R}_{sat}^{(n)}\Big|_{\eta=\eta_c}, \vec{R}_{\Delta r} \right\rangle \Big/ \left(n! \cdot R_0\right). \tag{43}$$

Here, B_{n_ref} is the polynomial coefficient corresponding to the reference point, which is fixed.

APPENDIX II

The signal after LRWC is $s_{LRWC}(f_\tau,\eta)$, which is given by (8). Based on the principle of stationary phase (POSP), the signal in the 2-D frequency domain can be represented by

$$\begin{aligned} s_{LRWC}\left(f_\eta,f_\tau\right) &= \int_{-\infty}^{\infty} s_{LRWC}(f_\tau,\eta)\cdot\exp\left(-j2\pi f_\eta\eta\right)d\eta \\ &\approx \exp\left\{j\left[P_0\left(f_\eta,f_\tau\right)+P_1\left(f_\eta,f_\tau\right)R_{\Delta r}\right]\right\} \\ &\quad\times\exp\left(-j2\pi f_\eta\eta_c\right)\exp\left[j4\pi\left(f_\tau+f_0\right)r_{10}\eta_c/c\right] \end{aligned}, \quad (44)$$

where

$$\begin{aligned} P_0\left(f_\eta,f_\tau\right) &= \left[\theta\left(f_\eta,f_\tau\right)+2\pi f_\eta\eta_c-4\pi\left(f_\tau+f_0\right)r_{10}\eta_c/c\right]\Big|_{R_{\Delta r}=0} \\ &= -\frac{\pi f_\tau^{\,2}}{\gamma}-2\pi f_\eta\sum_{m=1}^{N-1}C_m\big|_{R_{\Delta r}=0}f_\eta^{\,m} \\ &\quad -\frac{4\pi\left(f_\tau+f_0\right)}{c}\left[r_{00}+\sum_{n=2}^{N}r_{n0}\left(\sum_{m=1}^{N-1}C_m\big|_{R_{\Delta r}=0}f_\eta^{\,m}\right)^n\right] \end{aligned}$$

$$\begin{aligned} P_1\left(f_\eta,f_\tau\right) &= \left.\frac{\partial\theta\left(f_\eta,f_\tau\right)}{\partial R_{\Delta r}}\right|_{R_{\Delta r}=0} \\ &= -\frac{4\pi\left(f_0+f_\tau\right)}{c}\sum_{n=0}^{N}r_{n1}\left(\sum_{m=1}^{N-1}C_m\big|_{R_{\Delta r}=0}f_\eta^{\,m}\right)^n \\ &\quad -\frac{4\pi\left(f_0+f_\tau\right)}{c}\sum_{n=1}^{N}nr_{n0}\left(\sum_{m=1}^{N-1}C_m\big|_{R_{\Delta r}=0}f_\eta^{\,m}\right)^{n-1}\sum_{m=1}^{N-1}\left(\left.\frac{\partial C_m}{\partial R_{\Delta r}}\right|_{R_{\Delta r}=0}f_\eta^{\,m}\right) \\ &\quad -\frac{8\pi\left(f_0+f_\tau\right)^2}{c^2}\sum_{n=1}^{N}r_{n0}n\left(\sum_{m=1}^{N-1}C_m\big|_{R_{\Delta r}=0}f_\eta^{\,m}\right)^{n-1}r_{11}\sum_{m=1}^{N-1}m\,C_m\big|_{R_{\Delta r}=0}f_\eta^{\,m-1} \\ &\quad -2\pi f_\eta\sum_{m=1}^{N-1}\left(\left.\frac{\partial C_m}{\partial R_{\Delta r}}\right|_{R_{\Delta r}=0}f_\eta^{\,m}\right)-\frac{4\pi\left(f_0+f_\tau\right)}{c}f_\eta r_{11}\sum_{m=1}^{N-1}m\,C_m\big|_{R_{\Delta r}=0}f_\eta^{\,m-1} \end{aligned}$$

and

$$\begin{cases} C_1=-\dfrac{c}{4\left(f_0+f_\tau\right)B_2} \\ C_2=-\dfrac{3B_3c^2}{32\left(f_0+f_\tau\right)^2B_2^{\,3}} \\ C_3=\dfrac{4B_2B_4c^3-9B_3^{\,2}c^3}{128\left(f_0+f_\tau\right)^3B_2^{\,5}} \\ C_4=\dfrac{-2B_5B_2^{\,2}c^4+12B_4B_2B_3c^4-13B_3^{\,3}c^4}{204\left(f_0+f_\tau\right)^4B_2^{\,7}} \\ C_5=\dfrac{2B_6B_2^{\,3}c^5-18B_5B_2^{\,2}B_3c^5-9B_2^{\,2}B_4^{\,2}c^5+75B_2B_3^{\,2}B_4c^5-56B_3^{\,4}c^5}{819\left(f_0+f_\tau\right)^5B_2^{\,9}} \end{cases}$$

Equation (44) is transformed into the wavenumber domain, leading to

$$\begin{aligned} s_{LRWC}\left(k_\eta,\Delta k_\tau\right) &\approx \exp\left\{j\left[P_0\left(k_\eta,\Delta k_\tau\right)+P_1\left(k_\eta,\Delta k_\tau\right)R_{\Delta r}\right]\right\} \\ &\quad\times\exp\left(-jk_\eta v\eta_c\right)\exp\left[j\left(k_{\tau c}+\Delta k_\tau\right)r_{10}\eta_c\right] \end{aligned}, \quad (45)$$

where $k_\eta=2\pi f_\eta/v$, $k_{\tau c}=4\pi f_0/\mathrm{c}$, and $\Delta k_\tau=4\pi f_\tau/c$.

APPENDIX III

By applying the Taylor expansion, $P_1\left(k_\eta,\Delta k_\tau\right)$ can be expressed as

$$P_1\left(k_\eta,\Delta k_\tau\right)=\sum_{h=0}^{H}\left[\frac{1}{h!}\cdot\left.\frac{\partial^h P_1\left(k_\eta,\Delta k_\tau\right)}{\partial\Delta k_\tau^{\,h}}\right|_{\Delta k_\tau=0}\cdot\Delta k_\tau^{\,h}\right]. \quad (46)$$

After Stolt interpolation, Δk_τ and $\left(k_{\tau c}+\Delta k_\tau'\right)$ satisfy the following equation:

$$\Delta k_\tau=\sum_{h=1}^{H}A_h\left[\left(k_{\tau c}+\Delta k_\tau'\right)-P_1\left(k_\eta,\Delta k_\tau\right)\big|_{\Delta k_\tau=0}\right]^h. \quad (47)$$

Therefore,

$$\begin{aligned} \Delta\Phi\left(k_\eta,\Delta k_\tau'\right) &= \exp\left[j\Delta k_\tau r_{10}\eta_c\right] \\ &= \exp\left[j\cdot\sum_{h=1}^{H}A_h\left[\left(k_{\tau c}+\Delta k_\tau'\right)-P_1\left(k_\eta,\Delta k_\tau\right)\big|_{\Delta k_\tau=0}\right]^h\cdot r_{10}\eta_c\right] \end{aligned}, \quad (48)$$

where

$$\begin{cases} A_1=\dfrac{1}{o_1} \\ A_2=-\dfrac{o_2}{o_1^3} \\ A_3=\dfrac{1}{o_1^5}\left(2o_2^2-o_1o_3\right) \\ A_4=-\dfrac{1}{o_1^7}\left(5o_2^3-5o_1o_2o_3+o_1^2r_4\right) \end{cases}$$

and

$$o_h=\frac{1}{h!}\cdot\left.\frac{\partial^h P_1\left(k_\eta,\Delta k_\tau\right)}{\partial\Delta k_\tau^{\,h}}\right|_{\Delta k_\tau=0}.$$

APPENDIX IV

Because

$$\left.\frac{\partial^2\Delta\Phi\left(k_\eta,\Delta k_\tau'\right)}{2\cdot\left(\partial k_\eta\right)^2}\right|_{\Delta k_\eta=0}\approx\frac{4\pi\cdot r_{21}r_{10}\eta_c}{100\cdot r_{20}^{\,2}\left(r_{01}-r_{10}r_{11}\big/2\cdot r_{20}\right)}, \quad (49)$$

which is substituted into (15), the following expressions can be obtained

$$\eta_c>\frac{25\cdot r_{20}^{\,2}\left(r_{01}-r_{10}r_{11}\big/2\cdot r_{20}\right)}{r_{21}B_\eta^{\,2}r_{10}} \quad (50)$$

and

$$L_{DOAF}=2\left|\eta_c\right|\cdot v<\frac{50\cdot r_{20}^{\,2}\left(r_{01}-r_{10}r_{11}\big/2\cdot r_{20}\right)v}{r_{21}B_\eta^{\,2}r_{10}}, \quad (51)$$

where B_η is the Doppler bandwidth.

REFERENCES

[1] J. C. Curlander, R. N. McDonough, *Synthetic Aperture Radar: Systems and Signal Processing*. New York, NY, USA: John Wiley & Sons, 1991.

[2] B. Liu, K. Wang, X. Liu, W. Yu, "Range Cell Migration Correction using texture mapping on GPU," in *IEEE 10th international conference on signal processing*, Beijing, China, 2010, pp. *2172-2175*.

[3] Q. Lu, K. Wang, X. Liu, and X. Guo, "An automatic RCMC technique based on BFGS method," in *IEEE International Geoscience and Remote Sensing Symposium (IGARSS)*, Beijing, China, 2016, pp. *1022-1025*.

[4] G. Xu, M. Xing, L. Zhang, and Z. Bao, "Robust Autofocusing Approach for Highly Squinted SAR Imagery Using the Extended Wavenumber Algorithm," in *IEEE Transactions on Geoscience and Remote Sensing*,

vol. *51*, no. *10*, pp. *5031-5046*, Oct. 2013, DOI. 10.1109/TGRS.2013.2276112.

[5] L. Zhang, J. Sheng, M. Xing, Z. Qiao, T. Xiong, and Z. Bao, "Wavenumber-Domain Autofocusing for Highly Squinted UAV SAR Imagery," in *IEEE Sensors Journal*, vol. *12*, no. *5*, pp. *1574-1588*, May 2012, DOI. 10.1109/JSEN.2011.2175216.

[6] G. W. Davidson, I. G. Cumming, and M. R. Ito, "A chirp scaling approach for processing squint mode SAR data," in *IEEE Transactions on Aerospace and Electronic Systems*, vol. *32*, no. *1*, pp. *121-133*, Jan. 1996, DOI. 10.1109/7.481254.

[7] G. W. Davidson, I. Cumming, "Signal properties of spaceborne squint-mode SAR," in *IEEE Transactions on Geoscience and Remote Sensing*, vol. *35*, no. *3*, pp. *611-617*, May 1997, DOI. 10.1109/36.581976.

[8] K. Wang, X. Liu, "Squint mode SAR imaging with range-walk removal," in *IEEE International Conference on Acoustics*, *Speech, and Signal Processing*, Philadelphia, PA, USA, 2005, pp. *1113-1116*.

[9] H. Zhong, Y. Zhang, Y. Chang, E. Liu, X. Tang, and J. Zhang, "Focus High-Resolution Highly Squint SAR Data Using Azimuth-Variant Residual RCMC and Extended Nonlinear Chirp Scaling Based on a New Circle Model," in *IEEE Geoscience and Remote Sensing Letters*, vol. *15*, no. *4*, pp. *547-551*, April 2018, DOI. 10.1109/LGRS.2018.2800105.

[10] G. Sun, X. Jiang, M. Xing, Z. Qiao, Y. Wu, and Z. Bao, "Focus Improvement of Highly Squinted Data Based on Azimuth Nonlinear Scaling," in *IEEE Transactions on Geoscience and Remote Sensing*, vol. *49*, no. *6*, pp. *2308-2322*, June 2011, DOI. 10.1109/TGRS.2010.2102040.

[11] S. Zhang, M. Xing, X. Xia, J. Li, R. Guo, and Z. Bao, "A Robust Imaging Algorithm for Squint Mode Multi-Channel High-Resolution and Wide-Swath SAR With Hybrid Baseline and Fluctuant Terrain," in *IEEE Journal of Selected Topics in Signal Processing*, vol. *9*, no. *8*, pp. *1583-1598*, Dec. 2015, DOI. 10.1109/JSTSP.2015.2464182.

[12] Z. Sun, J. Wu, Z. Li, Y. Huang, and J. Yang, "Highly Squint SAR Data Focusing Based on Keystone Transform and Azimuth Extended Nonlinear Chirp Scaling," in *IEEE Geoscience and Remote Sensing Letters*, vol. *12*, no. *1*, pp. *145-149*, Jan. 2015, DOI. 10.1109/LGRS.2014.2329554.

[13] M. Xing, Y. Wu, Y. D. Zhang, G. Sun, and Z. Bao, "Azimuth Resampling Processing for Highly Squinted Synthetic Aperture Radar Imaging With Several Modes," in *IEEE Transactions on Geoscience and Remote Sensing*, vol. *52*, no. *7*, pp. *4339-4352*, July 2014, DOI. 10.1109/TGRS.2013.2281454.

[14] J. Chen, H. Kuang, W. Yang, W. Liu, and P. Wang, "A Novel Imaging Algorithm for Focusing High-Resolution Spaceborne SAR Data in Squinted Sliding-Spotlight Mode," in *IEEE Geoscience and Remote Sensing Letters*, vol. *13*, no. *10*, pp. *1577-1581*, Oct. 2016, DOI. 10.1109/LGRS.2016.2598066.

[15] H. Kuang, J. Chen, and W. Yang, "A refined two-step algorithm for high resolution spaceborne SAR with squinted sliding spotlight mode," in *IEEE International Geoscience and Remote Sensing Symposium (IGARSS)*, Milan, Italy, 2015, pp. *4476-4479*.

[16] D. An, X. Huang, T. Jin, and Z. Zhou, "Extended Nonlinear Chirp Scaling Algorithm for High-Resolution Highly Squint SAR Data Focusing," in *IEEE Transactions on Geoscience and Remote Sensing*, vol. *50*, no. *9*, pp. *3595-3609*, Sept. 2012, DOI. 10.1109/TGRS.2012.2183606.

[17] G. Sun, Y. Wu, J. Yang, M. Xing, and Z. Bao, "Full-Aperture Focusing of Very High Resolution Spaceborne-Squinted Sliding Spotlight SAR Data," in *IEEE Transactions on Geoscience and Remote Sensing*, vol. *55*, no. *6*, pp. *3309-3321*, June 2017, DOI. 10.1109/TGRS.2017.2669205.

[18] Z. Li *et al.*, "A Modified Equivalent Range Model and Wavenumber-Domain Imaging Approach for High-Resolution-High-Squint SAR With Curved Trajectory," in *IEEE Transactions on Geoscience and Remote Sensing*, vol. *55*, no. *7*, pp. *3721-3734*, July 2017, DOI. 10.1109/TGRS.2017.2678763.

[19] P. Wang, W. Liu, J. Chen, M. Niu, and W. Yang, "A High-Order Imaging Algorithm for High-Resolution Spaceborne SAR Based on a Modified Equivalent Squint Range Model," in *IEEE Transactions on Geoscience and Remote Sensing*, vol. *53*, no. *3*, pp. *1225-1235*, March 2015, DOI. 10.1109/TGRS.2014.2336241.

[20] I. G. Cumming, F. H. Wong, *Digital Processing of Synthetic Aperture Radar Data: Algorithms and Implementation*. Norwood, MA, USA: Artech House, 2005.

[21] T. Zhang, Z. Ding, W. Tian, T. Zeng and W. Yin, "A 2-D Nonlinear Chirp Scaling Algorithm for High Squint GEO SAR Imaging Based on Optimal Azimuth Polynomial Compensation," in IEEE Journal of Selected Topics in Applied Earth Observations and Remote Sensing, vol. 10, no. 12, pp. 5724-5735, Dec. 2017, DOI. 10.1109/JSTARS.2017.2765353.

[22] D. Li, H. Lin, H. Liu, G. Liao, and X. Tan, "Focus Improvement for High-Resolution Highly Squinted SAR Imaging Based on 2-D Spatial-Variant Linear and Quadratic RCMs Correction and Azimuth-Dependent Doppler Equalization," in *IEEE Journal of Selected Topics in Applied Earth Observations and Remote Sensing*, vol. *10*, no. *1*, pp. *168-183*, Jan. 2017, DOI. 10.1109/JSTARS.2016.2569561.

[23] F. H. Wong, I. G. Cumming, and Y. L. Neo, "Focusing Bistatic SAR Data Using the Nonlinear Chirp Scaling Algorithm," in *IEEE Transactions on Geoscience and Remote Sensing*, vol. *46*, no. *9*, pp. *2493-2505*, Sept. 2008, DOI. 10.1109/TGRS.2008.917599.

[24] P. Zhou, M. Xing, T. Xiong, Y. Wang, and L. Zhang, "A Variable-Decoupling- and MSR-Based Imaging Algorithm for a SAR of Curvilinear Orbit," in *IEEE Geoscience and Remote Sensing Letters*, vol. *8*, no. *6*, pp. *1145-1149*, Nov. 2011, DOI. 10.1109/LGRS.2011.2158387.

[25] Z. Li, J. Wang, and Q. H. Liu, "Interpolation-Free Stolt Mapping for SAR Imaging," in *IEEE Geoscience and Remote Sensing Letters*, vol. *11*, no. *5*, pp. *926-929*, May 2014, DOI. 10.1109/LGRS.2013.2281847.

[26] S. Suzuki, Y. Osawa, Y. Hatooka, Y. Kankaku, and T. Watanabe, "Overview of Japan's Advanced Land Observing Satellite-2 mission," in *Proceedings of SPIE - The International Society for Optical Engineering*, Kyoto, Japan, 2009, 7474.

[27] X. Dong, S. Quegan, U. Yumiko, C. Hu, and T. Zeng, "Feasibility Study of C- and L-band SAR Time Series Data in Tracking Indonesian Plantation and Natural Forest Cover Changes," in *IEEE Journal of Selected Topics in Applied Earth Observations and Remote Sensing*, vol. 8, no. 7, pp. 3692-3699, July 2015, DOI. 10.1109/JSTARS.2015.2400439.

[28] C. Hu, Y. Li, X. Dong, R. Wang, and D. Ao, "Performance Analysis of L-Band Geosynchronous SAR Imaging in the Presence of Ionospheric Scintillation," in *IEEE Transactions on Geoscience and Remote Sensing*, vol. 55, no. 1, pp. 159-172, Jan. 2017, DOI. 10.1109/TGRS.2016.2602939.

[29] W. Xu, Y. Deng, P. Huang and R. Wang, "Full-Aperture SAR Data Focusing in the Spaceborne Squinted Sliding-Spotlight Mode," in *IEEE Transactions on Geoscience and Remote Sensing*, vol. *52*, no. *8*, pp. *4596-4607*, Aug. 2014, DOI. 10.1109/TGRS.2013.2282863.